ORIGINAL ARTICLE

lajss.org Latin American Journal of Solids and Structures

www.lajss.org

Analysis of Stress, Strain and Young's Modulus of Specimens under Propagation of the 1D Linear Elastic Stress Waves

Qi Minju[a], Zhou Xuan[b], Wu Yiding[b], Gao Guangfa[b*]

[a] School of Computer Science, Huainan Normal University, Anhui, China. Email: 526274106@qq.com

[b] School of Mechanical Engineering, Nanjing University of Science and Technology, Nanjing, China. Emails: zhoux@njust.edu.cn, yidingwu@njust.edu.cn, gfgao@ustc.edu.cn, gfgao@ustc.edu.cn

* Corresponding author

https://doi.org/10.1590/1679-78257848

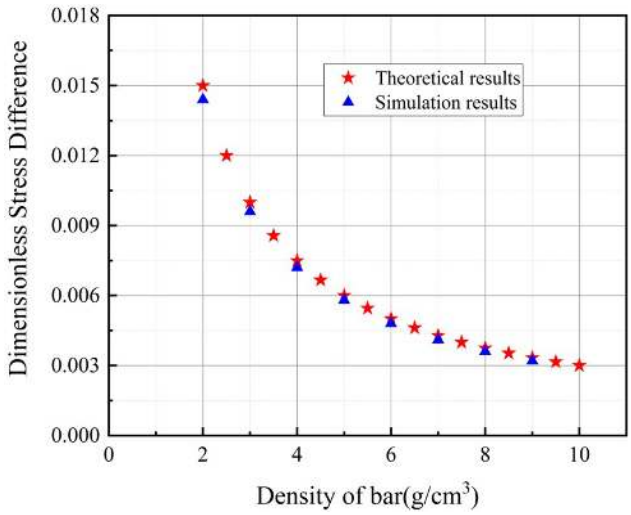
Abstract

The meticulous design and data processing of the SHPB test necessitate an exact analysis of the elastic segment to ensure an accurate acquisition of dynamic parameters. When other conditions align with theoretical requirements, a pressing question arises: Is the Young's modulus obtained through the stress wave theory while processing SHPB test data accurate? This is an issue that must be clearly addressed. To tackle this question, analytical expressions for parameters such as stress difference and particle velocity difference were derived. This allowed for the analysis of curve characteristics, influencing factors, and their underlying mechanisms. Building on this, equations for determining Young's modulus were deduced. The research indicates that when the wave impedance ratio is relatively large, the Young's modulus provided by the "two-wave method" inherently has a significant theoretical error. However, when the incident wave is sufficiently gradual, the Young's modulus deduced by the "three-wave method" proves to be remarkably accurate.

Keywords

Split Hopkinson Pressure Bar; Stress waves; Young’s modulus; Dynamical properties of materials

Graphical Abstract



Received: September 28, 2023. In revised form: October 06, 2023. Accepted: October 19, 2023. Available online: October 25, 2023
https://doi.org/10.1590/1679-78257848

Latin American Journal of Solids and Structures. ISSN 1679-7825. Copyright © 2023. This is an Open Access article distributed under the terms of the Creative Commons Attribution License, which permits unrestricted use, distribution, and reproduction in any medium, provided the original work is properly cited.

1 INTRODUCTION

The Split Hopkinson Pressure Bar (SHPB) stands as the central apparatus for contemporary examinations into the dynamic compressive attributes of materials. Harnessing the SHPB allows for the acquisition of the uniaxial dynamic stress-strain relationships of materials. This subsequently elucidates the strain rate effect on material strength and its associated dynamic stress-strain correlations—a crucial step in the establishment of dynamic constitutive equations for materials[1,2].In contrast to the quasi-static uniaxial compression tests on materials, the evaluation of the elastic phase in SHPB experiments exhibits a considerably profound impact on data interpretation. Challenges such as stress wave dispersion in SHPB tests result in the phenomenological yield strain figures substantially overshooting their genuine counterparts. Herein, parameters extracted from the elastic phase decisively influence the computation of true stress, true plastic strain, and true plastic strain rate. This influence is especially pronounced when considering brittle materials like concrete or soil-based substrates[3,4].Moreover, a myriad of studies has incorporated the curve of the elastic phase when formulating the material's constitutive equations or delving into its viscoelastic properties. These analyses frequently discuss its viscoelastic characteristics and the so-called dynamic Young's modulus[5-9]. Yet, the validity of the Young's modulus drawn from SHPB test data has been a bone of contention. Without meticulous experimentation design, the derived Young's modulus often lacks accuracy. For the same specimen material under differing incident wave influences, variations can emerge. These discrepancies might not solely stem from the material's viscoelastic properties but could also be attributed to non-uniform axial forces or deformations induced by stress wave propagation or uneven viscous stress coupling. Any of these scenarios might result in a flawed perception of viscoelastic properties, suggesting that conventional SHPB experiments might lack the rigor to quantitatively study material viscoelastic effects[10-12] or qualitatively ascertain if a material exhibits viscoelastic traits[13-16].

Numerous factors can influence the calculation of Young's modulus in Split Hopkinson Pressure Bar (SHPB) experiments. For instance, the lateral inertia effect caused by the Poisson's ratio of the bars and specimens, the dispersion issue of stress waves, as well as the interface friction effect, among others. The impact of these factors is not considered in this article. Initially, we derive the analytical expressions of the reflected and transmitted waves based on elastic incremental waves. Following this, we utilize numerical simulation to analyze the uniformity of the axial stress in the specimen and its influencing law. Subsequently, we provide the analytical formula for the velocities of the points at both ends of the specimen. This allows us to examine the evolution characteristics of deformation, strain rate, and strain during dynamic compression. Finally, we combine the theoretical analytical expressions with numerical simulation to analyze the changing trends and accuracy of the phenomenological Young's modulus. This elucidates whether the Young's modulus of the specimen obtained from the stress wave in the bar during SHPB experiments is accurate, under what circumstances it is accurate, and what the influencing factors and mechanisms are - even if all other conditions reach the ideal state. This work thus provides a theoretical reference for the precise design of SHPB experiments.

2 Elastic Wave Theoretical Calculations in SHPB Testing of Linearly Elastic Specimens

Consider an SHPB setup where both the incident and transmitted bars are linear-elastic slender cylindrical rods in tight contact with a cylindrical specimen, which has the same diameter and is coaxial with the two rods. Assume that both the incident and transmitted bars are made of steel with a density ρ_b of 7.83g/cm^3 and a Young's modulus of 210GPa. The bars have a diameter D of 14.5mm and a Poisson's ratio of 0. The specimen, made of a linear-elastic material, has a density ρ_s of 4.00g/cm^3, the length is l_s , a diameter of 14.5mm, and a Poisson's ratio of 0. If the planar incident wave is as depicted in Figure 1, with a linearly increasing leading edge, the platform stress of the incident wave σ_0 is -15Mpa, and the leading edge wave has a length λ of 800mm.

Let us designate the moment the incident wave first reaches the left end of the specimen as the initial instant. During the rising edge phase, the stress increment of the incident wave at unitless time can be defined as:

$$\delta\sigma = \frac{\sigma_0}{\lambda} C_b t_0 = -\frac{15MPa}{800mm} C_b t_0 = -0.17MPa\ ,\ t_0 = \frac{2l_s}{C_s} \tag{1}$$

Here, λ represents the width of the rising edge segment in the incident wave, and C_b represents the speed of sound in the bar.

According to the linear elastic incremental wave theory [17], we can deduce that when $t = nt_0$ the stress on the left end of the specimen at time is:

$$\sigma_{nl}=(\delta\sigma)\cdot\sum_{m=1}^{n}\left[1-\left(\frac{1-k}{1+k}\right)^{2m-1}\right]\Rightarrow\bar{\sigma}_{nl}=\frac{C_b t_0}{\lambda}\left\{n-\frac{1-k^2}{4k}\left[1-\left(\frac{1-k}{1+k}\right)^{2n}\right]\right\} \tag{2}$$

In the above equation,

$$k=\frac{\rho_s C_s}{\rho_b C_b},\ \bar{\sigma}_{nl}=\frac{\sigma_{nl}}{\sigma_0} \tag{3}$$

Subsequently, we can provide an expression for the dimensionless stress $\bar{\sigma}_{tl}$ at the left end at any time t between two nodes:

$$\begin{cases}\sigma_{tl}=\dfrac{\sigma_0 C_b}{\lambda}\dfrac{2k}{1+k}t, & t\le t_0\\ \sigma_{tl}=\sigma_{nl}+\dfrac{\sigma_0 C_b}{\lambda}(t-nt_0)\left[1-\left(\dfrac{1-k}{1+k}\right)^{2n+1}\right], & nt_0<t\le(n+1)t_0\le\dfrac{\lambda}{C_b}\end{cases} \tag{4}$$

In the above equation,

$$t_0\le\frac{\lambda}{(n+1)C_b} \tag{5}$$

Coupling this with equation (2), we can derive:

$$\bar{\sigma}_{tl}=\frac{2l_s}{\lambda}\frac{C_b}{C_s}\left\{n-\frac{1-k^2}{4k}\left[1-\left(\frac{1-k}{1+k}\right)^{2n}\right]+(\bar{t}-n)\left[1-\left(\frac{1-k}{1+k}\right)^{2n+1}\right]\right\},\ n<\bar{t}\le n+1, n\ge 0 \tag{6}$$

In this equation,

$$\bar{\sigma}_{tl}=\frac{\sigma_{tl}}{\sigma_0},\ \bar{t}=\frac{t}{t_0} \tag{7}$$

In the above equation, C_s represents the one-dimensional speed of sound in the specimen material.Thus, the dimensionless reflected stress wave expression within the incident rod is rendered as:

$$\bar{\sigma}_R=-\frac{2l_s}{\lambda}\frac{C_b}{C_s}\left\{\frac{1-k^2}{4k}\left[1-\left(\frac{1-k}{1+k}\right)^{2n}\right]+(\bar{t}-n)\left(\frac{1-k}{1+k}\right)^{2n+1}\right\},\ n<\bar{t}\le n+1, n\ge 0 \tag{8}$$

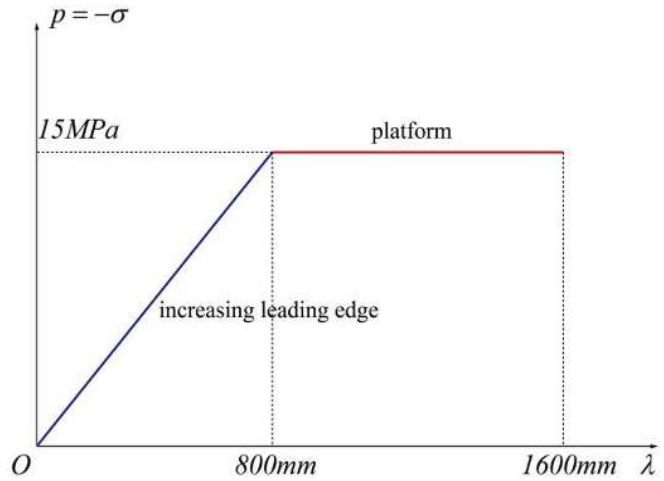


Figure 1: Schematic Illustration of the Incident Wave within the Incident Rod

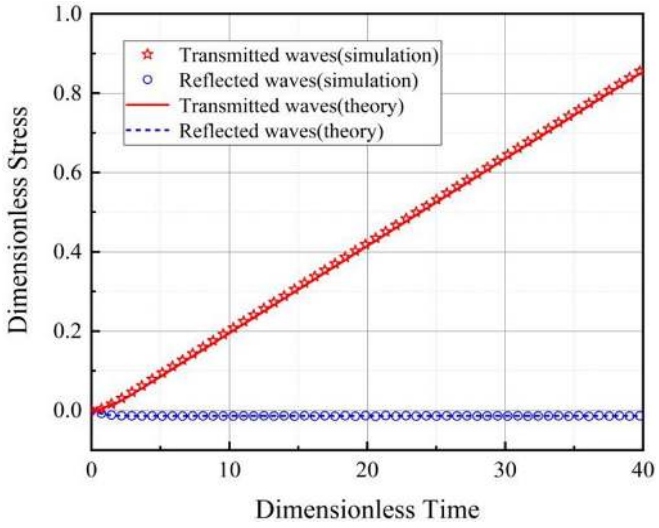


Figure 2: Comparison between Numerical Simulations and Theoretical Calculations of Dimensionless Reflected and Transmitted Waves

Similarly, we can determine the dimensionless transmitted wave $\bar{\sigma}_R$, that is, the dimensionless stress expression on the right $\bar{\sigma}_{tr}$ end:

$$\begin{cases} \bar{\sigma}_{tr} = 0, & \bar{t} \le \dfrac{1}{2} \\ \bar{\sigma}_{tr} = \dfrac{2l_s}{\lambda}\dfrac{C_b}{C_s}\left\{ n - \dfrac{(1-k)^2}{4k}\left[1-\left(\dfrac{1-k}{1+k}\right)^{2n}\right] + \left(\bar{t}-n-\dfrac{1}{2}\right)\left[1-\left(\dfrac{1-k}{1+k}\right)^{2n+2}\right]\right\}, & n+\dfrac{1}{2} < \bar{t} \le n+\dfrac{3}{2} \end{cases} \tag{9}$$

Leveraging the Abaqus software for simulation, a two-dimensional axisymmetric model was erected. Both the rod and the specimen conform to linear-elastic constitutive models. The axial dimension of the specimen's element is set at 0.25mm. From this simulation, the relative stress at both ends of the specimen was determined. Given a specimen length of 6mm and a Young's modulus of 50GPa, we can delineate the theoretical calculations and numerical simulation outcomes for the dimensionless reflected and transmitted waves, as depicted in Figure 2. The illustration attests to the robust congruence between theoretical and simulated results. Notably, when the dimensionless time exceeds 1.5, the simulation values for the transmitted wave are marginally and consistently higher than the theoretical values. This discrepancy primarily stems from data retrieval errors during the simulation, echoing the divergence observed between the simulated and theoretical stress difference elaborated later.

3 Uniformity Analysis of Stress at Both Ends of the Specimen and its Influencing Factors

Based on equations (6) and (9), the dimensionless stress difference at both ends of the specimen can be computed as:

$$\Delta\bar{\sigma}_t = \bar{\sigma}_{tl} - \bar{\sigma}_{tr} = \begin{cases} \Gamma\cdot\bar{t}, & \bar{t} \le \dfrac{1}{2} \\ \Gamma\cdot\left\{\dfrac{1}{4}\left[k+1+(k+3)\left(\dfrac{1-k}{1+k}\right)^{2n+1}\right] - \left(\dfrac{1-k}{1+k}\right)^{2n+1}(\bar{t}-n)\right\}, & n+\dfrac{1}{2} < t \le n+1 \\ \Gamma\cdot\left\{\dfrac{1+k}{4}\left[1-\left(\dfrac{1-k}{1+k}\right)^{2n+2}\right] + \left(\dfrac{1-k}{1+k}\right)^{2n+2}(\bar{t}-n-1)\right\}, & n+1 < t \le n+\dfrac{3}{2} \end{cases} \tag{10}$$

And

$$\Gamma = \frac{2l_s}{\lambda}\frac{C_b}{C_s}\frac{2k}{1+k} \tag{11}$$

Presuming a Young's modulus for the specimen to be 200GPa and a length of 6mm, the comparison graph between the theoretical values provided by equation (10) and the simulation results is illustrated in Figure 3. Both curves exhibit an analogous trend, progressively augmenting with the increase in dimensionless time. When the dimensionless time exceeds 2, the stress difference at both ends of the specimen approximates a constant. However, variances are evident. The theoretical curve linearly ascends when the dimensionless specimen is less than 0.5, subsequently stabilizing post fluctuations. In contrast, the simulation curve displays a smooth arching ascent devoid of peak oscillations. Analyses indicate that such variations predominantly arise from numerical simulation inaccuracies, rather than theoretical computation discrepancies. During the numerical simulation, even though an ideal linearly augmenting incident wave, as shown in Figure 1, is inputted, the effects of artificial viscosity in numerical simulation calculations invariably induce a smoothing at the abrupt angular transition points. While this nuance might be negligible for the entire loading process, as Figure 3 reveals, around a dimensionless time of 3, the stress difference at both ends of the specimen essentially plateaus to an almost constant value. The disparities between the theoretical and simulated outcomes within these three dimensionless times are evident when zooming into the ideal input curve and simulation curve for incident waves within this time frame, as displayed in Figure 4. This dispersion-like effect, wrought by artificial viscosity, manifests an arc transition phase in the incident wave. Consequently, the slope of the incident wave $\sigma(\bar{t})$ during this phase is markedly less than the ideal and varies over time.

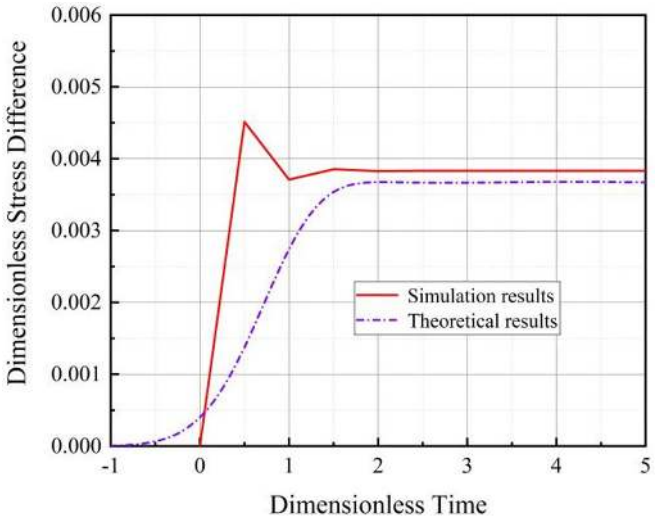


Figure 3: Comparative Analysis of Theoretical and Simulated Results for Stress Difference at Both Ends of the Specimen

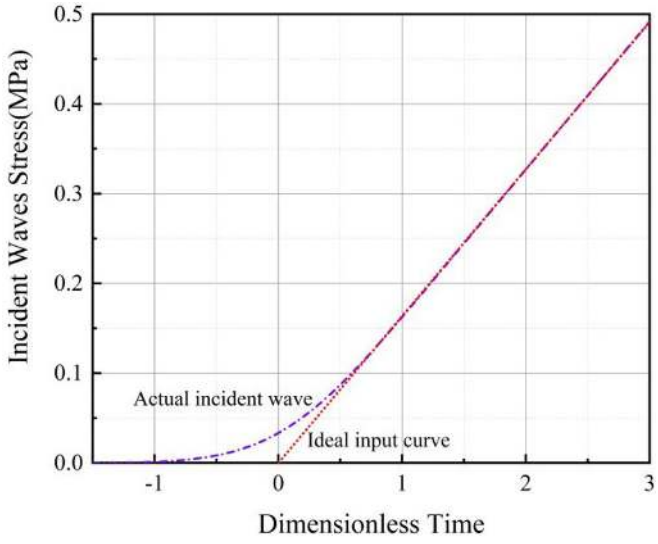


Figure 4: Comparison between Two Algorithmic Calculations and Simulation for Stress Difference at Both Ends of the Specimen

Based on the actual incident wave values presented in Figure 4, and through the application of stress wave theory, we can deduce the dimensionless stress expression for both ends of the specimen when the dimensionless time does not exceed 4.

$$\sigma_{tl}=\begin{cases}\sigma\left(\bar{t}\right)\cdot\dfrac{2k}{1+k}, & \bar{t}\le 1\\ \dfrac{2k}{1+k}\left[\sigma\left(\bar{t}\right)+\displaystyle\sum_{i=1}^{n}\sigma\left(\bar{t}-i\right)\cdot\frac{2(1-k)^{2i-1}}{(1+k)^{2i}}\right], & n<\bar{t}\le n+1\end{cases} \tag{12}$$

And

$$\sigma_{tr}=\begin{cases}0, & \bar{t}\le\dfrac{1}{2}\\ \dfrac{4k}{(1+k)^2}\displaystyle\sum_{i=1}^{n}\sigma\left(\bar{t}-\frac{2i-1}{2}\right)\cdot\left(\frac{1-k}{1+k}\right)^{2i-2}, & \dfrac{2n-1}{2}<\bar{t}\le\dfrac{2n+1}{2}\end{cases} \tag{13}$$

The theoretical curve for the stress difference at both ends of the specimen, as derived from this, is visualized in Figure 5. From the figure, it is evident that when theoretical calculations are applied using the incident wave on the left end of the specimen from the simulation, the rising phase of the stress difference curve essentially overlaps with the simulated curve. Any oscillations within this are obfuscated by the arc buffering segment. This means that if the incident wave were ideally linearly increasing, there would be evident oscillations as shown in Figure 3. This parameter, due to the minimal dimensionless time required for the stress difference to reach its steady state, masks this feature through the arc phase of the incident wave.If we keep all other parameters of the rod and specimen constant and reduce the Young's modulus of the specimen to 25GPa, the impedance ratio, k, subsequently diminishes. The required dimensionless time to reach the steady state extends. The resulting dimensionless stress difference curves for both ends of the specimen are illustrated in Figure 6. Notably, irrespective of theoretical calculations or numerical simulations, significant oscillations in the stress difference are observed before arriving at an approximately steady state. However, due to the arc transition introduced by the artificial viscosity in numerical simulation, the oscillation magnitude is relatively subdued.

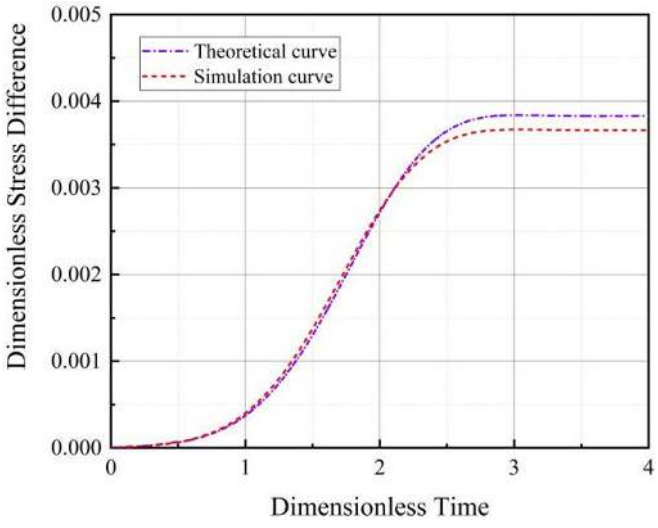


Figure 5: Comparison between Theoretical Calculations and Simulated Curves under Actual Simulated Incident Waves

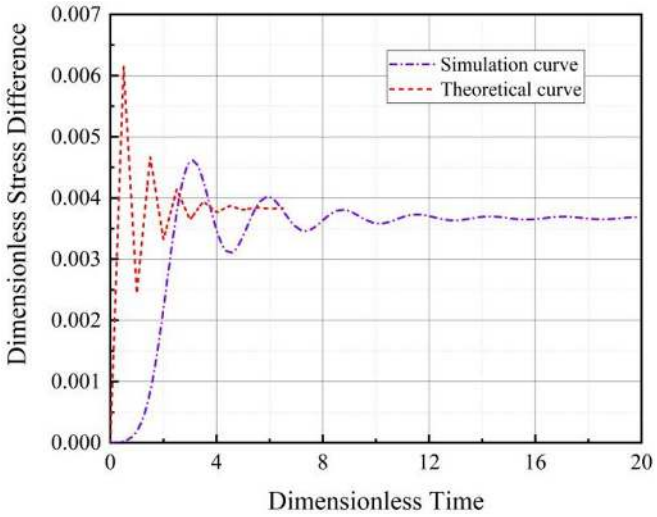


Figure 6: Theoretical and Simulated Comparison for Young's Modulus of 25GPa

From Figure 3, it is evident that both the numerical simulation outcomes and the theoretical computations reveal that as the dimensionless time increases, the stresses at both ends of the time axis converge to a steady value. As per Equation (10), when n is considerably large, the dimensionless stress difference between the left and right ends of the specimen can be approximated as:

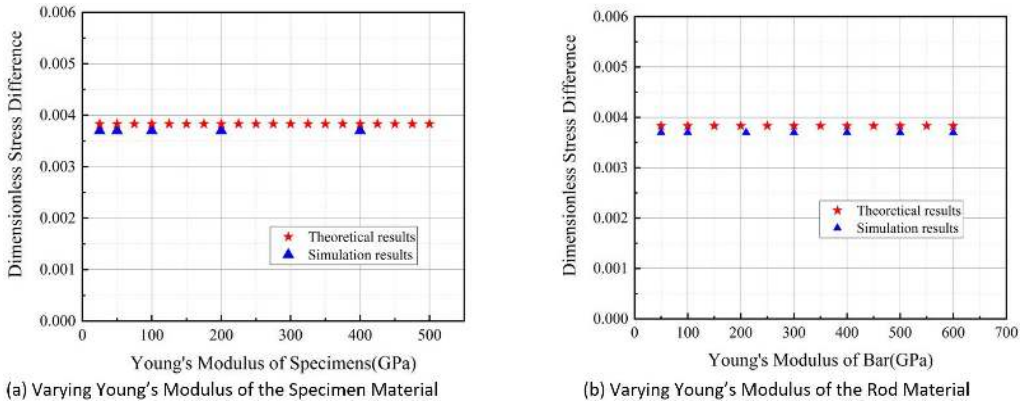
$$\Delta\bar{\sigma}_t \approx \frac{kC_b t_0}{2\lambda} = \frac{l_s \rho_s}{\lambda \rho_b} \tag{14}$$

This implies that given specific lengths of the specimen, incident wave wavelengths, and densities of both the specimen and rod, the dimensionless stress difference remains approximately constant. Yet, as discerned from Figure 3, regardless of whether one employs the ideal linear incident wave or the actual incident wave on the specimen's left end from the simulation, theoretical calculations slightly exceed the simulated values. The core challenge lies in the numerical simulation. As delineated by Equation (14), the stress difference correlates positively with the specimen's length. Both the theoretical and simulation models designate the specimen's length as 6mm. However, in the actual simulation modeling, the axial length of each element is 0.25mm. Since the stress integration points are centrally located in each element, the stress values retrieved from the simulation for the left and right ends of the specimen, in a strict sense, pertain to the nodes at 0.125mm and 5.875mm, respectively. Consequently, the effective length of the simulated specimen is 5.75mm. Based on theoretical calculations, specifically Equation (14), the steady value of the dimensionless stress difference is approximately 0.00383. After adjusting for the specimen length, the simulation's steady state value should approximate 0.00367, aligning closely with the 0.0036695 value presented in Figure 3. As the axial length of the specimen element in the simulation model decreases, its steady state value increasingly converges with the theoretical result. For an element size of 0.10mm, reducing the specimen element length from 0.25mm to 0.10mm results in a simulated steady state value of 0.0037668. Employing the correction method yields a simulated value of 0.003766 based on theoretical calculations. Therefore, this analysis corroborates the precision of the expressions proffered by the theoretical exploration.

Equation (14) elucidates that during the stable phase with a linearly increasing incident wave, the dimensionless stress difference between both ends of the specimen is independent of the Young's modulus of either the specimen or rod. Thus, it remains uninfluenced by the sonic velocity of the rod or material. This is graphically substantiated in Figure 7. Regardless of the Young's modulus variations for the rod or specimen, both simulation and calculation results consistently validate this principle.

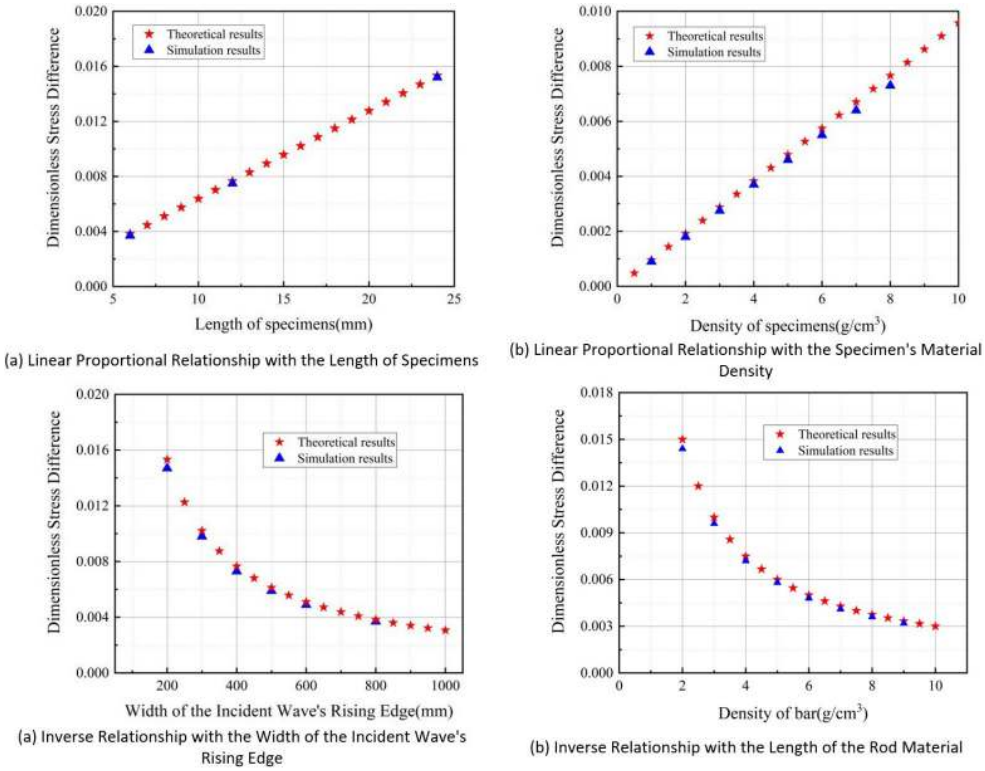
Furthermore, from the equation, one can deduce that with a linear incident wave, the steady value interval of the dimensionless stress difference between both ends of the specimen is directly proportional to the specimen's length and density. Conversely, it's inversely proportional to the width of the incident wave's rising edge and the rod's density. This aligns seamlessly with the simulation outcomes showcased in Figure 8.

Additionally, based on Equation (14), given a specific ratio of specimen length to the width of the linear incident wave's rising edge, and a defined ratio of densities between the specimen and rod materials, the value of the dimensionless stress difference in its steady state is determinate. This is aptly exemplified by the comparisons between theoretical analyses and simulation results as depicted in Figures 9 and 10.



(a) Varying Young's Modulus of the Specimen Material (b) Varying Young's Modulus of the Rod Material

Figure 7: Comparative Results of Dimensionless Stress Difference in Simulation and Theoretical Calculation for Different Rod or Specimen Materials with Varying Young's Modulus



(a) Linear Proportional Relationship with the Length of Specimens

(b) Linear Proportional Relationship with the Specimen's Material Density

(a) Inverse Relationship with the Width of the Incident Wave's Rising Edge

(b) Inverse Relationship with the Length of the Rod Material

Figure 8: Influencing Factors and Trends for the Constant Interval of Dimensionless Stress Difference at Both Ends of the Specimen

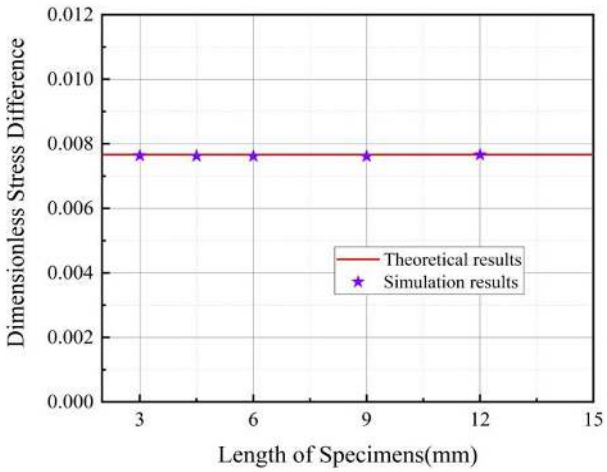


Figure 9: Comparative Analysis between Numerical Simulations and Theoretical Calculations of Dimensionless Stress Difference at Both Ends of the Specimen for a Specimen Length to Incident Wave Length Ratio of 6:800

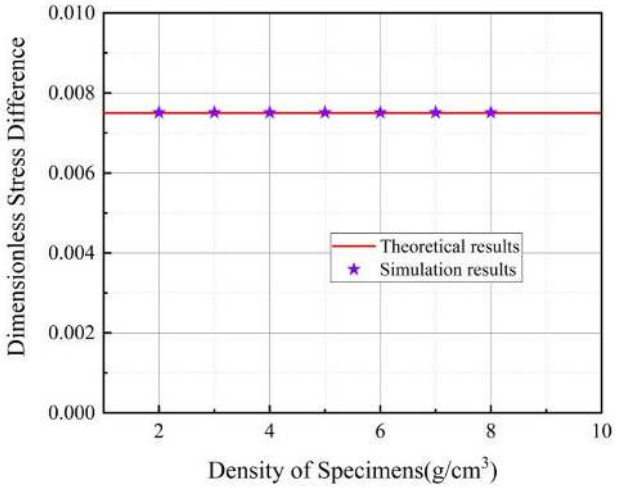


Figure 10: Comparison between Theoretical Calculations and Numerical Simulations of Dimensionless Stress Difference at Both Ends for Different Material Densities with a Density Ratio of 1

Although parameters such as Young's modulus of the specimen and the rod material do not influence the magnitude of the dimensionless stress difference at the constant value region, they markedly influence the time it takes for the dimensionless stress difference to reach this near-constant region.

4 Analysis of the Specimen's Deformation, Strain Rate, and Strain, Along with their Influencing Factors

Building upon the stress curves at both ends of the specimen, the velocity of the particles on the left end surface of the specimen at time $t = nt_0$ can be ascertained using the motion equation on the wavefront of the elastic incremental wave [17]:

$$v_{nl} = \left(\frac{\delta\sigma}{\rho_b C_b}\right)\cdot\sum_{m=1}^{n}\left\{\left[1-\left(\frac{1-k}{1+k}\right)^{2m-1}\right]-1\right\}+\sum_{m=1}^{n}\left(-\frac{\delta\sigma}{\rho_b C_b}\right)=-\frac{\sigma_0 t_0}{\lambda\rho_b}\left\{n+\frac{1-k^2}{4k}\left[1-\left(\frac{1-k}{1+k}\right)^{2n}\right]\right\} \tag{15}$$

By similar logic, the particle velocity on the right end surface of the specimen during the rising edge loading phase at time $t = \left(n+1/2\right)t_0$ can be determined as:

$$v_{(n+1/2)r} = -\left(\frac{\delta\sigma}{\rho_b C_b}\right)\cdot\sum_{m=1}^{n}\left[1-\left(\frac{1-k}{1+k}\right)^{2m}\right] \tag{16}$$

Subsequently, through interpolation, the particle velocities on the end surfaces of the specimen at any given time t can be computed as follows:

$$v_{tl} = -\frac{2l_s}{\lambda}\frac{\sigma_0}{\rho_b C_s}\left\{\bar{t}+\left(\bar{t}-n\right)\left(\frac{1-k}{1+k}\right)^{2n+1}+\frac{1-k^2}{4k}\left[1-\left(\frac{1-k}{1+k}\right)^{2n}\right]\right\},\quad n<\bar{t}\le n+1 \tag{17}$$

And

$$\begin{cases} v_{tr}=0, & \bar{t}\le\dfrac{1}{2} \\ v_{tr} = -\dfrac{2l_s}{\lambda}\dfrac{\sigma_0}{\rho_b C_s}\left\{\bar{t}-\left(\bar{t}-n\right)\left(\dfrac{1-k}{1+k}\right)^{2n+2}-\dfrac{1+k^2}{4k}+\dfrac{1+4k+k^2}{4k}\left(\dfrac{1-k}{1+k}\right)^{2n+2}\right\}, & n+\dfrac{1}{2}<\bar{t}\le n+\dfrac{3}{2} \end{cases} \tag{18}$$

Consequently, the difference in particle velocities between the left and right ends of the specimen is:

$$\Delta v_t = v_{tl} - v_{tr}$$
$$= \begin{cases} -\dfrac{2l_s}{\lambda}\dfrac{\sigma_0}{\rho_b C_s}\dfrac{2\bar{t}}{1+k}, & \bar{t} \le \dfrac{1}{2} \\ -\dfrac{2l_s}{\lambda}\dfrac{\sigma_0}{\rho_b C_s}\left\{(\bar{t}-n)\dfrac{2}{1+k}\left(\dfrac{1-k}{1+k}\right)^{2n+1} + \dfrac{1}{2k} - \dfrac{1}{2k}\dfrac{3k+1}{1-k}\left(\dfrac{1-k}{1+k}\right)^{2n+2}\right\}, & n+\dfrac{1}{2} < \bar{t} \le n+1 \\ -\dfrac{2l_s}{\lambda}\dfrac{\sigma_0}{\rho_b C_s}\left\{(\bar{t}-n)\dfrac{2}{1+k}\left(\dfrac{1-k}{1+k}\right)^{2n+2} + \dfrac{1}{2k} - \dfrac{1}{2k}\dfrac{5k+1}{1+k}\left(\dfrac{1-k}{1+k}\right)^{2n+2}\right\}, & n+1 < \bar{t} \le n+\dfrac{3}{2} \end{cases} \quad (19)$$

Taking specimens with Young's modulus values of 400GPa, 200GPa, 100 GPa, 50 GPa, and 25 GPa as illustrations, the velocity differences calculated from the above formula juxtaposed against those derived from simulations are depicted in Figure 11. The graph demonstrates that in all five scenarios, the velocity difference between the left and right ends oscillates from zero, increasing until it stabilizes at a near-constant value. For portions of the constant and rising regions, the theoretical computations are consistent with the simulation results.

Figure 11 manifests that regardless of whether the outcomes are from theoretical computations or numerical simulations, when the dimensionless time is sufficiently large, the velocity difference between the two ends of the specimen transitions into a stable region. According to Equation (19), when n is large, the velocity difference can be approximated as:

$$\Delta v_t = -\frac{\sigma_0}{\lambda}\frac{l_s C_b}{\rho_s C_s^{\,2}} \quad (20)$$

The results derived from the aforementioned equation compared against the numerical simulation results are presented in Figure 12. It is evident from the graph that the theoretical calculations align seamlessly with the simulation outcomes.

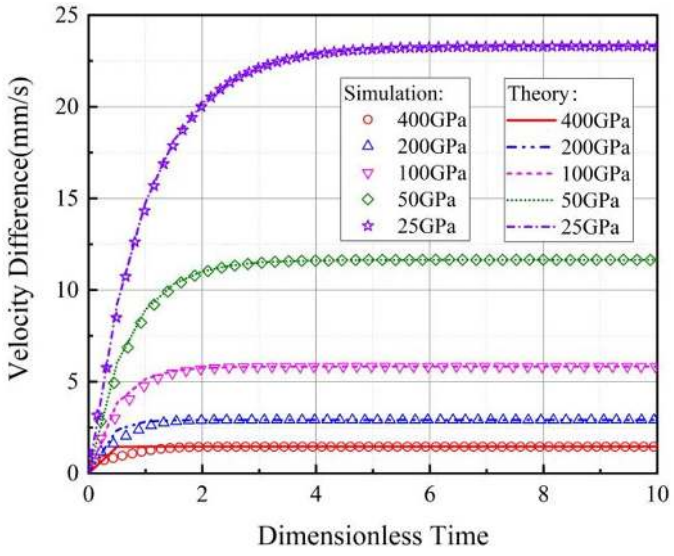


Figure 11: Theoretical Calculation and Simulation Results for Velocity Difference at Both Ends of the Specimen

Moreover, Figure 11 also illustrates that the starting point of the time at which the velocity difference of the specimen's particle reaches the constant value region differs based on Young's modulus. As Young's modulus increases, the corresponding dimensionless time progressively decreases. This phenomenon is explicable by Equation (19), which demonstrates that the closer the impedance of the specimen and rod material is to 1, the closer the computed result of the equation is to Equation (20)—essentially approaching a constant value, implying a diminished required dimensionless time.

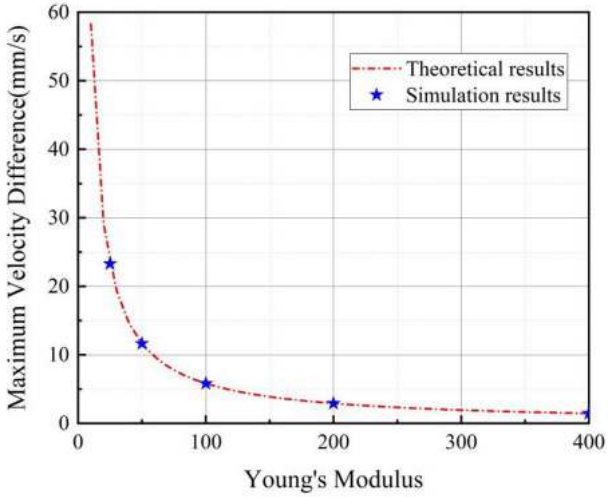


Figure 12: Maximum Velocity Difference Theoretical Calculations and Simulations for Different Young's Modulus

According to Equation (19), the strain rate of the specimen can be calculated as:

$$\dot{\varepsilon}=-\frac{\Delta v_t}{l_s}=\begin{cases}\dfrac{2}{\lambda}\dfrac{\sigma_0}{\rho_b C_s}\dfrac{2\bar{t}}{1+k}, & \bar{t}\le\dfrac{1}{2}\\ \dfrac{2}{\lambda}\dfrac{\sigma_0}{\rho_b C_s}\left\{(\bar{t}-n)\dfrac{2}{1+k}\left(\dfrac{1-k}{1+k}\right)^{2n+1}+\dfrac{1}{2k}-\dfrac{1}{2k}\dfrac{3k+1}{1-k}\left(\dfrac{1-k}{1+k}\right)^{2n+2}\right\}, & n+\dfrac{1}{2}<\bar{t}\le n+1\\ \dfrac{2}{\lambda}\dfrac{\sigma_0}{\rho_b C_s}\left\{(\bar{t}-n)\dfrac{2}{1+k}\left(\dfrac{1-k}{1+k}\right)^{2n+2}+\dfrac{1}{2k}-\dfrac{1}{2k}\dfrac{5k+1}{1+k}\left(\dfrac{1-k}{1+k}\right)^{2n+2}\right\}, & n+1<\bar{t}\le n+\dfrac{3}{2}\end{cases} \tag{21}$$

When the velocity difference between the two ends of the specimen reaches the constant value region, the above equation can be approximated as:

$$\dot{\varepsilon}=\frac{\sigma_0}{\lambda}\frac{C_b}{\rho_s C_s{}^2} \tag{22}$$

5 Analysis of the Accuracy of the Experimental Young's Modulus Calculated Using the Stress Wave Method

Employing Equations (6) and (9)—the "three-wave method" in SHPB data processing—one can determine the specimen's average dimensionless axial stress:

$$\overline{\bar{\sigma}_t}=\frac{\bar{\sigma}_{tl}+\bar{\sigma}_{tr}}{2}=$$
$$\begin{cases}\dfrac{2l_s}{\lambda}\dfrac{C_b}{C_s}\dfrac{k}{1+k}\bar{t}, & \bar{t}\le\dfrac{1}{2}\\ \dfrac{2l_s}{\lambda}\dfrac{C_b}{C_s}\left\{n+\dfrac{1}{2}-\dfrac{1}{4k}+\dfrac{1}{4k}\left(\dfrac{1-k}{1+k}\right)^{2n+1}+\left[1-\dfrac{1}{1+k}\left(\dfrac{1-k}{1+k}\right)^{2n+1}\right]\left(\bar{t}-n-\dfrac{1}{2}\right)\right\}, & n+\dfrac{1}{2}<\bar{t}\le n+1\\ \dfrac{2l_s}{\lambda}\dfrac{C_b}{C_s}\left\{n+1-\dfrac{1}{4k}+\dfrac{1}{4k}\left(\dfrac{1-k}{1+k}\right)^{2n+2}+\left[1-\dfrac{1}{1+k}\left(\dfrac{1-k}{1+k}\right)^{2n+2}\right](\bar{t}-n-1)\right\}, & n+1<\bar{t}\le n+\dfrac{3}{2}\end{cases} \tag{23}$$

Using the above equation, the average axial stress of specimens with Young's modulus values of 200GPa and 25GPa was calculated, and the resulting curves are illustrated in Figure 13. It's evident from Figure 13 that the theoretical computations and numerical simulation results are virtually congruent. In the initial phase of the stress wave impinging

on the specimen, the average stress of the specimen does not linearly increase like the incident wave. Instead, it nonlinearly ascends, with its slope gradually amplifying until it aligns with that of the incident wave. The time required for a specimen with a Young's modulus of 25GPa to transition to the linearly increasing phase is noticeably longer than for one with a Young's modulus of 200GPa.

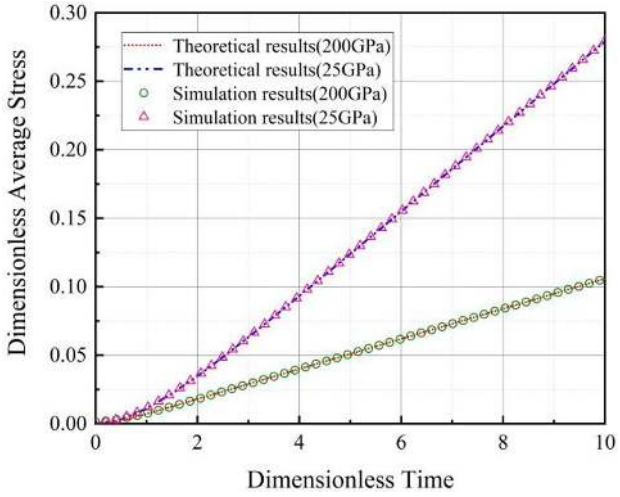


Figure 13: Comparative Analysis between Theoretical Calculations and Numerical Simulations of the Average Stress at Both Ends of the Specimen

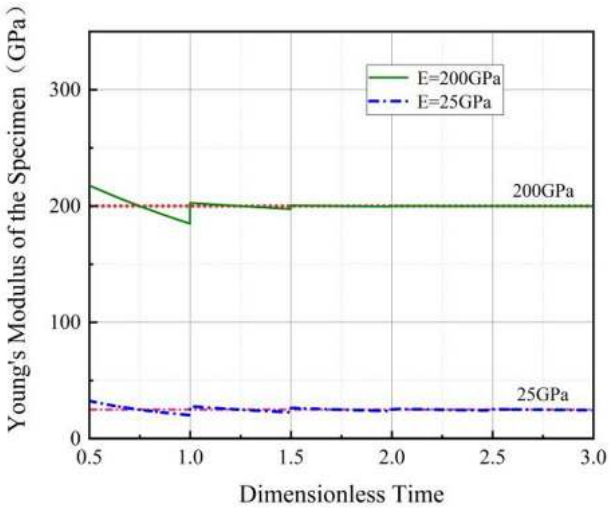


Figure 14: Experimental Young's Modulus of the Specimen Based on the "Three-wave Method" versus Actual Value

Thus, employing the "three-wave method", the experimental Young's modulus of the specimen can be determined as:

$$E=\frac{d\sigma}{d\varepsilon}=\frac{\overline{\sigma_t}'}{\dot{\varepsilon}}=\begin{cases}\dfrac{\rho_s C_s^{\,2}\left[1-\dfrac{1}{1+k}\left(\dfrac{1-k}{1+k}\right)^{2n+1}\right]}{1+\left(\bar{t}-n\right)\dfrac{4k}{1+k}\left(\dfrac{1-k}{1+k}\right)^{2n+1}-\dfrac{3k+1}{1-k}\left(\dfrac{1-k}{1+k}\right)^{2n+2}}, & n+\dfrac{1}{2}<\bar{t}<n+1 \\ \dfrac{\rho_s C_s^{\,2}\left[1-\dfrac{1}{1+k}\left(\dfrac{1-k}{1+k}\right)^{2n+2}\right]}{1+\left(\bar{t}-n\right)\dfrac{4k}{1+k}\left(\dfrac{1-k}{1+k}\right)^{2n+2}-\dfrac{5k+1}{1+k}\left(\dfrac{1-k}{1+k}\right)^{2n+2}}, & n+1<\bar{t}<n+\dfrac{3}{2}\end{cases} \tag{24}$$

Utilizing the aforementioned equations, the time-course curve of the experimental Young's modulus calculated via the "three-wave method" for different specimen Young's moduli can be ascertained, as illustrated in Figure 14. As observed

from the figure, when n exceeds 3, the experimental Young's modulus approximates a constant value. However, when n is less than 0.5, the discrepancy between the experimental Young's modulus and its actual value is profound, rendering it unsuitable as a reference. For a dimensionless time n ranging from 0.5 to 3, oscillations around the actual value are evident, neither consistently surpassing nor remaining beneath it. Yet, as dimensionless time increases, these oscillations diminish until the experimental Young's modulus closely mirrors the actual value. In essence, if the slope of the incident wave's ascending phase is sufficiently minute, enabling numerous back-and-forths of the elastic wave within the specimen and thereby ensuring a sufficiently large dimensionless time, the equation can be approximated as:

$$E = \rho_s C_s^{\,2} = E_s \tag{25}$$

Under these stipulated conditions, the "three-wave method" can accurately deduce the Young's modulus, where E_s represents the actual Young's modulus of the specimen material.

Considering the Young's modulus at the corresponding point $\overline{t} = n$, the modulus deduced from the "three-wave method" simplifies to:

$$\overline{E} = \frac{E_n}{E_s} = \frac{1-\left(\dfrac{1-k}{1+k}\right)^{2n+1}}{1-(1+k)^2\left(\dfrac{1-k}{1+k}\right)^{2n+1}} \tag{26}$$

In the context of SHPB, the generalized wave impedance ratio is typically less than 1, which means the dimensionless experimental Young's modulus derived from the equation generally exceeds 1. Hence, when the incident wave is a linearly increasing compression wave, the Young's modulus calculated using the "three-wave method" slightly exceeds the actual modulus. However, when n is sufficiently large, this discrepancy becomes negligible.

Assuming that the dimensionless experimental modulus does not exceed K as previously analyzed, K generally exceeds 1 and is regarded as accurate, then the minimum value for the dimensionless time n can be approximated as:

$$n_{\min} = \frac{1}{2}\left[\ln\frac{K-1}{K(1+k)^2-1} \Big/ \ln\left(\frac{1-k}{1+k}\right) - 1\right] \tag{27}$$

For instance, if K is taken to be 1.001, indicating a relative error of 0.1%, the minimum dimensionless time required to obtain an accurate Young's modulus for varying wave impedance ratios of the specimen and rod materials is shown in Figure 15. This graph reveals a non-linear decrease in the required minimum dimensionless time as the wave impedance ratio approaches 1.

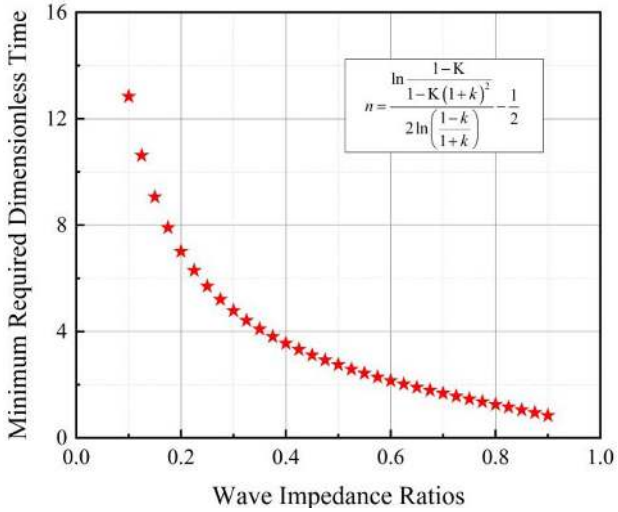


Figure 15: Minimum Required Dimensionless Time for Different Wave Impedance Ratios

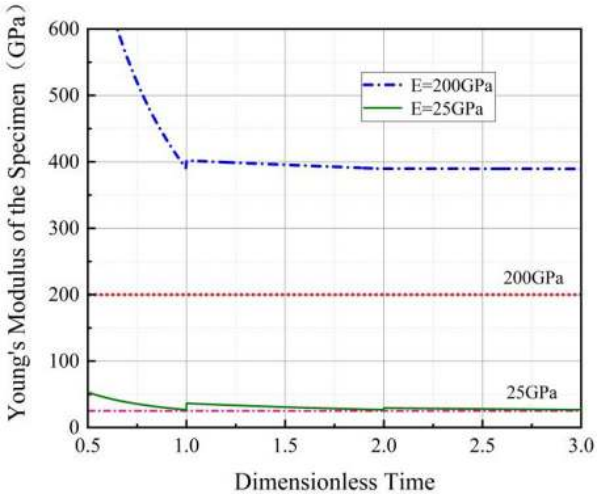


Figure 16: Experimental Young's Modulus of the Specimen Calculated Using the "Two-wave Method" versus Actual Value

For K set at 1.01, representing a threshold relative error of 1%, and using RHA armor steel as an example with a material density of 7.85g/cm^3, a one-dimensional elastic yield strength of 792MPa, and a quasi-static Young's modulus of approximately 209GPa, with a rod diameter of 14.5mm, and specimen diameter and length of 5mm and 3mm respectively—the specimen can be virtually equated to the rod diameter. The equivalent wave impedance ratio between the virtual specimen and the rod stands at 0.12, with an equivalent yield strength of 94MPa. According to Equation (27), the minimum absolute time width is 14.67μs, implying that the maximum slope of the incident wave linear ascending phase should be less than 6.41MPa/μs.

Taking concrete as another example and utilizing an SHPB system with a diameter of 80mm, a specimen diameter of 70mm, a length of 40mm, a quasi-static compressive strength of 60MPa, a Young's modulus of 30GPa, and a density of 2.4g/cm^3, the resultant minimum approximate time width is around 114.27μs. This means the maximum slope of the incident wave's linear ascending phase should be less than 0.53MPa/μs. However, in SHPB experiments, using a 14.5mm steel rod as a reference and an impact speed of around 15m/s, the average slope of the incident wave's ascending phase surges to 27 MPa/μs. Consequently, the Young's modulus obtained in SHPB tests for concrete specimens without tailored wave-shaping design is typically imprecise.

Utilizing the "two-wave method" based on the "reflected wave + transmitted wave" to calculate the specimen's Young's modulus, one can similarly derive the expression for the experimental Young's modulus.

$$E=\frac{\rho_b C_s C_b\left[1-\left(\frac{1-k}{1+k}\right)^{2n+2}\right]}{4\left(\bar{t}-n\right)\left(\frac{1-k}{1+k}\right)^{2n+1}+\frac{1-k^2}{k}\left[1-\left(\frac{1-k}{1+k}\right)^{2n}\right]},\qquad n<\bar{t}<n+1, t>\frac{1}{2} \tag{28}$$

For illustration, let's consider specimen Young's moduli of 200GPa and 25GPa. The comparison between the computed results and the actual values is depicted in Figure 16. As observed from Figure 16, when the dimensionless time n is less than 2, there's a notable fluctuation in the experimental Young's modulus over time, with the amplitude for the 25GPa specimen being markedly lesser than that for the 200GPa specimen. However, when n exceeds 2, the experimental dimensionless modulus gradually stabilizes to a constant value.

For considerably large values of dimensionless time n, the equation can be simplified to:

$$E=\frac{\rho_s C_s^{\ 2}}{1-k^2}=\frac{E_s}{1-k^2} \tag{29}$$

In contrast to the "three-wave method", even when the dimensionless time is adequately large, the experimental Young's modulus invariably surpasses the actual value. As illustrated in Figure 16, for a specimen Young's modulus of 200GPa, the experimental modulus is 389.649GPa, which is 1.948 times the actual modulus. Conversely, for a specimen modulus of 25GPa, the experimental modulus is 26.619GPa, amounting to 1.0648 times the actual modulus. Hence, when the ascending segment of the incident wave is sufficiently gradual and the wave impedance ratio (or generalized wave impedance ratio) between the specimen and the rod material is minimized, the Young's modulus calculated via the "two-wave method" becomes increasingly precise.

6 Conclusion

The Split Hopkinson Pressure Bar (SHPB) test stands as one of the paramount methodologies currently employed to evaluate the dynamic mechanical properties of materials. The underpinnings of this experimental test rest on the one-dimensional stress theory and two foundational assumptions. When juxtaposed against quasi-static uniaxial tests, the elastic phase in SHPB experiments reveals considerably heightened intricacy, with a plethora of influencing variables. The analysis and determination of this elastic phase profoundly impact the scientific validity and accuracy of parameters such as dynamic yield strength, true stress, true plastic strain, true strain rate, and even the constitutive relationships. This study predominantly delves into the scientific veracity and precision of the experimental Young's modulus derived from SHPB tests using the stress wave method, under theoretical conditions and when presented with a semi-trapezoidal incident wave, eschewing other influences like lateral inertial effects or end-face friction. The salient conclusions are as follows:

Analytical solutions for stress and particle velocity on both ends of the specimen were delineated. Precise solutions for the reflected and transmitted waves under the aegis of a linear incident wave were derived, and these theoretical computations were juxtaposed with numerical simulations, thereby affirming the veracity of our quantitative analysis. A mathematical representation delineating the stress difference at both ends of the specimen under a linear incident wave was presented. Through harmonizing theoretical curves with numerical simulation results, the temporal stress difference dynamics, key influencing factors, and their operational patterns were elucidated. Theoretical outcomes were further validated through practical examples and numerical simulations.

Expressions depicting the velocity difference, which translates to axial deformation, during stress wave propagation were deduced. The primary factors and their underlying mechanisms affecting the strain rate and strain alteration characteristics during the testing process were meticulously parsed. Numerical simulations were deployed to probe the oscillation processes in the preliminary deformation stage of specimens with diverse material parameters and subsequently, the characteristics of their steady-state domains.

The analytical expression for the specimen's experimental Young's modulus, derived through the "three-wave method" under ideal conditions, was presented. Analysis evinced that if the dimensionless width of the incident wave's rising edge is below a specific threshold, the Young's modulus derived from the SHPB test through the "three-wave method" cannot be reliably referenced. A steeper incident wave implies augmented inaccuracies. This implies that to attain a relatively accurate experimental Young's modulus, the slope of the incident wave must remain below a critical value. Concurrently, this critical dimensionless width exhibits a conspicuous functional relationship with the impedance ratio, for which an approximate analytical expression has been proposed. Subsequent analysis of the Young's modulus expression derived through the "two-wave method" indicated that, aside from the problem of substantial inaccuracies at widths below the critical dimensionless time, when the impedance ratio isn't exceedingly minuscule, even with a vast elastic width of the incident wave, the resultant Young's modulus is marred by non-trivial errors.

Acknowledgments

The author(s) disclose the receipt of the following financial support for the research, authorship, and/or publication of this article: The project was supported by the National Natural Science Foundation of China (Grant No: 12172179, 11772160, 11472008).

Author's Contribuitions: Conceptualization, QI Minju and ZHOU Xuan; Methodology, ZHOU Xuan; Investigation, GAO Guangfa and WU Yiding; Writing - original draft, QI Minju, ZHOU Xuan and GAO Guangfa; Writing - review & editing, GAO Guangfa; Funding acquisition, GAO Guangfa; Resources, ZHOU Xuan and QI Minju; Supervision, GAO Guangfa.

Editor: Marcílio Alves

References

1. Alaghmandfard R., Dharmendra C., Odeshi A.G., Mohammadi M. Dynamic mechanical properties and failure characteristics of electron beam melted Ti-6Al-4V under high strain rate impact loadings[J]. Materials Science & Engineering A 793 (2020) 139794. https://doi.org/10.1016/j.msea.2020.139794.

2. Wu X., Jiang F. C., Wang Z. Q., Yuan D., Gao G. H., Guo C. H. Mechanical behavior and microstructural evolution of a bainite-based quenching-partitioning (BQ&P) steel under high strain rates[J]. Materials Science & Engineering A 818 (2021) 141414. https://doi.org/10.1016/j.msea.2021.141414

3. Soares G. C., Hokka M.The Taylor–Quinney coefficients and strain hardening of commercially pure titanium, iron, copper, and tin in high rate compression[J]. International Journal of Impact Engineering 156 (2021) 103940. https://doi.org/10.1016/j.ijimpeng.2021.103940.

4. Zhu Z. W., Ning J. G., Liu X. Dynamic Mechanical Behaviors of Soil under Impact Loads[J]. Chinese Journal of High Pressure Physics, 2011, 25(5): 444-450. (in Chinese).

5. Chen J. P., Tao W. J., Huan S., Xu C. Data processing of wave propagation in viscoelastic split Hopkinson pressure bar[J]. AIP Advances 12, 045210 (2022); https://doi.org/10.1063/5.0083888.

6. Zhou Z. P., Gao D. D., Lin G. J., Sun W. F. Static and dynamic mechanical properties of epoxy nanocomposites reinforced by hybridization with carbon nanofibers and block ionomers[J]. Engineering Fracture Mechanics 271 (2022) 108638. https://doi.org/10.1016/j.engfracmech.2022.108638

7. Rotariu A.-N., Tranˇa E., Matache L. Young's Modulus Calculus Using Split Hopkinson Bar Tests on Long and Thin Material Samples[J]. Materials 2022, 15, 3058. https://doi.org/10.3390/ma15093058.

8. Aghayan S., Bieler S., Weinberg K. Determination of the high-strain rate elastic modulus of printing resins using two different split Hopkinson pressure bars[J]. Mechanics of Time-Dependent Materials (2021) 26:761–773. https://doi.org/10.1007/s11043-021-09511-2.

9. Zhang Q., Huang X., Guo R., Chen D. Study on Dynamic Impact Response and Optimal Constitutive Model of Al-Mg-Si Aluminum Alloy. Materials 2022, 15, 7618. https://doi.org/10.3390/ma15217618.

10. Sun W. X., Luo Z. H., Tang M. F., Li M. Liu T. Zhang D. G. Compressive mechanical properties and constitutive relations of PBX-1[J].Explosion and Shock Waves, 2019, 39(7): 072301. (in Chinese)

11. Lei J. F.,Xu M., Liu T., Xuan Y., Sun H., Wei Z. Static/dynamic mechanical properties and a constitutive model of a polyvinyl chloride elastomer[J].Explosion and Shock Waves, 2020, 40(10): 103103. (in Chinese)

12. Huang R. Y., Yu P. S., Liu Y., Tian C. L., Chang J. Y., Wang P. F., Zhao J. H. Study on the visco-hyperelastic behavior of polysiloxane rubber[J]. Chinese Journal of Theoretical and Applied Mechanics, 2021, 53(1): 184-193 .(in Chinese)

13. Prakash G., Singh N.K., Gupta N.K. Flow behaviour of Ti-6Al-4V alloy in a wide range of strain rates and temperatures under tensile, compressive and flexural loads[J]. International Journal of Impact Engineering, 176 (2023): 104549. https://doi.org/10.1016/j.ijimpeng.2023.104549

14. Zhai Y., Li N.,Zhao J. H., Wang S. W. Stress wave propagation in damage nonlinear elastic rock materials specimen during SHPB tests[J].Journal of Xi'an University of Architecture &Technology (Natural Science Edition), 2015,47(3): 359-363. (in Chinese)

15. Tao J. L., Li K. A thermo-viscoelastic rate-dependent constitutive equation for cement mortar with damage[J]. Explosion and Shock Waves, 2011, 31(3): 268-273. (in Chinese)

16. Du R. F., Pei X. J., Jia J., Zhang X. C., Chen J. Y., Zhang G. H. Viscoelastic damage constitutive relation of sandstone under multiple impact load[J]. Journal of Jilin University (Engineering and Technology Edition), 2021, 51(2): 638-649. (in Chinese)

17. Gao G. F. Introduction to Stress Waves in Solid. Beijing: Science Press, 2022: 211-219. (in Chinese).